

Synthesis of large and homogeneous single crystals of water-bearing minerals by slow cooling at deep-mantle pressures

TAKUO OKUCHI^{1,*}, NARANGOO PUREVJAV¹, NAOTAKA TOMIOKA^{1,†}, JUNG-FU LIN², TAKAHIRO KURIBAYASHI³, LOUISE SCHONEVELD^{4,‡}, HUIJEONG HWANG⁵, NAOYA SAKAMOTO⁶, NORIYUKI KAWASAKI⁷ AND HISAYOSHI YURIMOTO⁷

¹Institute for Study of the Earth's Interior, Okayama University, Misasa, Tottori 682-0193, Japan

²Department of Geological Sciences, Jackson School of Geosciences, University of Texas at Austin, Austin, Texas 78712-0254, U.S.A.

³Department of Earth Science, Graduate School of Science, Tohoku University, Sendai 980-8578, Japan

⁴School of Earth and Environmental Sciences, James Cook University, Townsville, Queensland 4811, Australia

⁵Department of Earth System Sciences, Yonsei University, Seoul 120-749, Korea

⁶Creative Research Institution, Hokkaido University, Sapporo, 001-0021, Japan

⁷Department of Natural History Sciences, Hokkaido University, Sapporo, 060-0810, Japan

ABSTRACT

The presence of water in the Earth's deep mantle is an issue of increasing interest in the field of high-pressure mineralogy. An important task for further advancing research in the field is to create homogeneous single crystals of candidate deep-mantle water-bearing minerals of 1 mm or larger in size, which is required for applying them for the time-of-flight (TOF) single-crystal Laue diffraction method with a third-generation neutron instrument. In this study, we perform several experiments to demonstrate an improved methodology for growing hydrous crystals of such large sizes at relevant transition zone and lower-mantle conditions via very slow cooling over a maximum period of 1 day. Successfully synthesized crystals using this methodology include dense hydrous magnesium silicate (DHMS) phase E, hydrous wadsleyite, hydrous ringwoodite, and bridgmanite (silicate perovskite). It is also demonstrated that these hydrous crystals can be grown from deuterium enriched starting materials in addition to those having a natural hydrogen isotope ratio.

Magnitudes of chemical and crystallographic heterogeneities of the product crystals were characterized by comprehensive analysis of X-ray precession photography, single-crystal X-ray diffraction (SCXRD), field-emission scanning electron microscope (FE-SEM), electron probe microanalyzer (EPMA), secondary ion mass spectroscopy (SIMS), powder X-ray diffraction (PXRD), and TOF neutron powder diffraction (TOF-NPD). The product crystals were confirmed to be inclusion free and crystallographically homogeneous. Compositional and isotopic differences of major elements and hydrogen isotope abundances were lower than 1 and 3%, respectively, among intracrystals and intercrystals within each recovered sample capsule. Phase E crystals up to 600 μm in the largest dimension were grown at a constant temperature of 1100 $^{\circ}\text{C}$ kept for 3 h. Using a lattice parameter-to-temperature relation of phase E, the thermal gradient in the sample capsules for the phase E synthesis has been evaluated to be 20 $^{\circ}\text{C}/\text{mm}$. Hydrous wadsleyite crystals up to 1100 μm in the largest dimension were grown at 1390 $^{\circ}\text{C}$ with a temperature reduction of 70 $^{\circ}\text{C}$ during heating for 10 h. Hydrous ringwoodite crystals up to 1000 μm in the largest dimension were grown at around 1400 $^{\circ}\text{C}$ with a temperature reduction of 110 $^{\circ}\text{C}$ during heating for 12 h. Bridgmanite crystals up to 600 μm in the largest dimension were grown at 1700 $^{\circ}\text{C}$ with a temperature reduction of 30 $^{\circ}\text{C}$ during heating for 12 h. A TOF single-crystal diffraction instrument has been successfully used for analyzing one of the hydrous wadsleyite crystals, which demonstrated that single crystals appropriate for their expected usage are created using the method proposed in the present study.

Keywords: Hydrous minerals, single-crystal growth, phase E, wadsleyite, ringwoodite, bridgmanite, slow-cooling method

INTRODUCTION

Water, an essential component of the Earth, exists in surface oceans and in deep-mantle hydrous minerals (Inoue et al. 1995; Kanzaki 1991; Kohlstedt et al. 1996; Litasov et al. 2003; Pearson

et al. 2014). Recent research has suggested that part of the oceanic water is being transported into the deep mantle through the subducting lithosphere to affect the Earth's global dynamic and chemical cycles (Bercovici and Karato 2003; Ohtani et al. 2004; Schmandt et al. 2014). In the Earth's early evolution, primordial water was partitioned among deep-mantle minerals, silicate melt, and metallic Fe alloy (Bolfan-Casanova et al. 2000; Inoue et al. 2010; Okuchi 1997; Shibazaki et al. 2009). Both processes transported water, which partitioned into the deep-mantle minerals, affecting the relevant mantle redox state (McCammon et al. 2004; Mrosko et al. 2013; Smyth et al. 2014). The existence of

* E-mail: okuchi@misasa.okayama-u.ac.jp

† Present address: Kochi Institute for Core Sample Research, Japan Agency for Marine-Earth Science and Technology, Nankoku, 783-8502 Kouchi, Japan.

‡ Present address: Research School of Earth Science, Australian National University, Canberra, ACT, 2602 Australia.

such water has been partly confirmed by a recent discovery of natural hydrous ringwoodite with 1.4 wt% water occurring as an inclusion in a diamond specimen (Pearson et al. 2014). This discovery indicates that at least some areas of the transition zone are enriched with a significant amount of water.

Hydrous deep-mantle minerals contain water as hydroxyl groups (Keppler and Smyth 2006). Numerous experimental results indicate that the physical properties of the host minerals change dramatically with an increase in hydroxyl concentration. These properties include melting behavior (Inoue 1994; Schmandt et al. 2014), phase relations (Ghosh et al. 2013; Ohtani et al. 2000), transformation kinetics (Kubo et al. 1998), rheology (Chen et al. 1998), and sound velocities (Inoue et al. 1998; Mao et al. 2011, 2012). An important task for further advancing the research on the effects of these hydroxyls is to create well-characterized, homogeneous, hydrous crystals of at least 1 mm in size. This is the minimum size requirement to use the time-of-flight (TOF) single-crystal Laue diffraction method with a third-generation neutron instrument such as TOPAZ at the Spallation Neutron Source (SNS) (Schultz et al. 2014). Using this state-of-the-art instrument will enable for the first time accurate determination of the position and occupancy of normal hydrogen atoms in the crystal structures of deep-mantle minerals, and therefore direct observation of chemical bonding distance and charge substitution mechanisms of the hydrogen. Moreover, accurate atomic displacement parameters of the hydrogen can be measured with this instrument for crystals 1 mm or larger (Jorgensen et al. 2014). These parameters provide invaluable information about chemical bonding strength and directionality of the hydrogen, which is essential for understanding and forecasting how hydroxyls control the physical properties of minerals.

In the present study, therefore, we synthesized such crystals of hydrous wadsleyite and hydrous ringwoodite, which are highly expected to occur or have been confirmed within the mantle transition zone. In addition, we synthesized dense hydrous magnesium silicate (DHMS) phase E with a deuterium-enriched composition in crystals up to 600 μm in size, which is a representative hydrous mineral that may occur in hydrated deep-mantle peridotite (Kanzaki 1991; Ohtani et al. 2004). Although the crystal size is smaller than 1 mm, it may be applicable for TOF single-crystal diffraction because deuterium scatters neutrons more coherently and induces much less background than normal hydrogen, for which the required crystal volume is smaller (Wenk 2006). Moreover, the deuterium-enriched crystals will be useful for investigating the hydrogen isotope fractionation phenomena occurring within the deep mantle (Chakoumakos et al. 2013; Horita et al. 2010; Okuchi et al. 2014; Yang et al. 2014). In addition to the DHMS phase E, therefore, ringwoodite crystals were also synthesized in a deuterium-enriched growth environment. Finally, lower-mantle bridgmanite (silicate perovskite) crystals 100 to 600 μm in size were synthesized in normal water (H_2O)-bearing growth environments. Although we were unable to grow these bridgmanite crystals into suitable sizes for TOF single-crystal diffraction, some proved to be ideal for use in advanced high-pressure–high-temperature X-ray and laser experiments (e.g., Goncharov et al. 2015).

It is reasonable to expect that crystals grown into larger sizes may become less homogeneous. We therefore consider that it is important to evaluate the chemical and crystallographic heteroge-

neity of the synthesized crystals. For this purpose, the crystals were comprehensively analyzed using X-ray precession photography, single-crystal X-ray diffraction (SCXRD), field-emission scanning electron microscope (FE-SEM), electron probe microanalyzer (EPMA), secondary ion mass spectroscopy (SIMS), powder X-ray diffraction (PXRD), and TOF neutron powder diffraction (TOF-NPD). In particular, we made a special effort to evaluate the hydrogen and deuterium concentration distributions within each crystal and among the crystals within each capsule of the selected run charges.

EXPERIMENTAL STRATEGY

Previous studies of high-pressure syntheses of deep-mantle crystals have partly addressed the aforementioned research task (Ito and Weidner 1986; Jacobsen et al. 2004; Shatskiy et al. 2007, 2009; Smyth et al. 2003). Of particular interest are crystals of ringwoodite up to 800 μm in size (Jacobsen et al. 2004; Smyth et al. 2003), and those of wadsleyite and bridgmanite up to 1 mm in size (Shatskiy et al. 2007, 2009). Most of these crystals were grown over a relatively short period of within a few hours. For the latter two products, the chemical gradients were intentionally introduced in addition to an existing thermal gradient (≥ 20 $^\circ\text{C}/\text{mm}$) under the extreme pressure–temperature environments of the sample capsules in which the crystals were quickly grown over short periods between 20 min to 3 h, except for one run at 5 h. Although these gradients played very essential roles in the successful synthesis of large and isometric crystals in short periods, they may also induce crystallographic heterogeneities due to fast growth, including lattice defects, crystal inclusions, twinning, and misorientation (Rudolph 2010), which were observed to exist within some of the crystals (Shatskiy et al. 2009). To apply the TOF single-crystal diffraction method, samples having these crystallographic heterogeneities are not very appropriate (Wenk 2006).

In the present study, we used a significantly slower growth rate over a maximum period up to 24 h to produce the sample crystals. In addition, we grew the crystals from a homogeneous silicate melt batch with a volume as large as possible to enable continuous buffering of the crystal's chemical composition. The temperature of the cell slowly decreased during the long heating durations so that the crystals were almost kept in chemical equilibrium with the silicate melt throughout the growth process. This slow-cooling method has been reported as an effective scheme for recovering large and homogeneous crystals of metal oxides from limited sample volumes confined at high pressures up to 11 GPa (Loeffert et al. 2002; Shatskiy et al. 2010; Tamura et al. 1974). In the present study, we extended this method to higher pressures and temperatures of up to 24 GPa and about 1800 $^\circ\text{C}$, respectively, for the crystal growth of deep-mantle hydrous mineral phases.

EXPERIMENTAL METHODS

DHMS phase E, pure magnesian hydrous wadsleyite, and pure magnesian and iron-bearing hydrous ringwoodite were synthesized at pressures between 14 and 21 GPa and temperatures between 1100 and 1400 $^\circ\text{C}$. Bridgmanite with three different compositions was synthesized at 24 GPa and 1650 to 1760 $^\circ\text{C}$. Table 1 shows a summary of these experimental conditions yielding relatively large crystal products. We used the scaled-up Kawai-type cell installed at the Institute for Study of the Earth's Interior at Okayama University (Shatskiy et al. 2011). Two different types of cell assembly designs suitable for two different pressure regimes were prepared. Fujillo F08 tungsten carbide anvils with 8 or 6 mm in truncation edge length (TEL) were used to compress these cells, which commonly had $\text{MgO-Cr}_2\text{O}_3$ pressure media of 14 mm in the octahedral edge length (OEL) (Fig. 1). Anvils 46 mm in size were used for applied loads of more than 10 MN, and those 32 mm in size were used for loads of less than 10 MN. The efficiency of the pressure generated by using these applied loads was previously calibrated for the combination of 14 mm OEL and 8 or 6 mm TEL (Frost et al. 2004; Shatskiy et al. 2009, 2011). Figure 1a shows a cross section of the cell coupled with 8 mm TEL, which was used for the phase E, wadsleyite, and ringwoodite synthesis. This cell design was established in our previous work for mass production of fully deuterated ringwoodite powder (Purevjav et al. 2014a). In the present study, the same gold capsule of 4 mm in diameter and 5 mm in length in this cell, with ~ 50 mm^3 in sample volume, was successfully used for the significantly longer heating durations required for single-crystal growth. Figure 1b shows the cross section of the other cell coupled with 6 mm TEL, which was used for the bridgmanite synthesis. This capsule was designed and tested to be highly durable at temperatures of at least up to 1800 $^\circ\text{C}$, at which the required long-duration runs were conducted in a stable manner. A platinum capsule of 2 mm in diameter and 4

TABLE 1. Experimental conditions and the maximum size of the recovered crystals

Run no.	Target phase	OEL/TEL (mm)	Load (MN)	P (GPa)	T (°C)	Duration (hours)	Starting materials	Size (µm)	Silicate melting
PE01	phase E	14/8	6.5	14	1100/1090	2	Mg ₂ SiO ₄ + 22 wt% D ₂ O	500	No
PE02	phase E	14/8	6.5	14	1100/1100	3	Mg ₂ SiO ₄ + 22 wt% D ₂ O	600	No
EP13-2	Mg wadsleyite	14/8	8.5	17	1300/1250	13	Mg ₂ SiO ₄ + 10 wt% H ₂ O	600	Yes
EP13-1	Mg wadsleyite	14/8	8.5	17	1400/1300	6	Mg ₂ SiO ₄ + 10 wt% H ₂ O	600	Yes
HW7	Mg wadsleyite	14/8	8.5	17	1400/1310	24	Mg ₂ SiO ₄ + 10 wt% H ₂ O	400	Yes
HW8	Mg wadsleyite	14/8	8.5	17	1400/1360	6	Mg ₂ SiO ₄ + 15 wt% H ₂ O	800	Yes
HW18	Mg wadsleyite	14/8	8.5	17	1390/1320	10	Mg ₂ SiO ₄ + 15 wt% H ₂ O	1100	Yes
HR14	Mg ringwoodite	14/8	19	21	1340/1310	1.5	Mg ₂ SiO ₄ + 5 wt% D ₂ O	200	Yes
HR12	Mg ringwoodite	14/8	19	21	1360/1360	2.5	Mg ₂ SiO ₄ + 11 wt% D ₂ O	600	Yes
EP13-3	Mg ringwoodite	14/8	19	21	1400/1290	12	Mg ₂ SiO ₄ + 10 wt% H ₂ O	1000	Yes
EP12-6	MgFe ringwoodite	14/8	9.6	18	1270/1260	1	(Mg _{0.91} Fe _{0.09}) ₂ SiO ₄ + 10 wt% H ₂ O	300	Yes
5k2247	Mg bridgmanite	14/6	19	24	1710/1650	3	Mg _{1.4} SiO _{3.4} + 9 wt% H ₂ O	200	Yes
5k2221	Mg bridgmanite	14/6	19	24	1700/1700	8	Mg _{1.3} SiO _{3.3} + 7 wt% H ₂ O	300	Yes
5k2174	MgFe bridgmanite	14/6	19	24	1650/1650	5.5	(Mg _{0.92} Fe _{0.08}) _{1.5} SiO _{3.5} + 6 wt% H ₂ O	100	Yes
5k2417	MgFe bridgmanite	14/6	19	24	1700/1670	12	(Mg _{0.84} Fe _{0.16}) _{1.8} SiO _{3.8} + 7 wt% H ₂ O	600	Yes
5k2179	MgFeAl bridgmanite	14/6	19	24	1760/1750	7	(Mg _{0.92} Fe _{0.08}) _{1.5} SiO _{3.5} + 0.2Al ₂ O ₃ + 5 wt% H ₂ O	100	Yes

mm in length, with ~12 mm³ in sample volume, was successfully used at even higher temperatures than those used in previous bridgmanite growth experiments (Ito and Weidner 1986; Shatskiy et al. 2007). The melt fraction and the chemical transport efficiency simultaneously increased at the higher temperatures at which we expected more homogeneous crystals to grow.

The starting materials were weighted mixtures of the components suitable for each synthesis (Table 1). Magnesium hydroxide [Mg(OH)₂], aluminum oxide [Al₂O₃], iron [Fe], and its oxide [FeO] were prepared from commercial reagents. Part of the iron and its oxide were enriched in ⁵⁷Fe for the expected applications in Mössbauer spectroscopy and nuclear resonant inelastic X-ray scattering. Silica [SiO₂] was prepared from a high-purity fused silica rod. Magnesium deuterioxide [Mg(OD)₂] was prepared by using a hydrothermal reaction of MgO powder and D₂O in an autoclave (Okuchi et al. 2014). For all runs except for EP12-6, the starting materials were the mixtures of these reagents, where H₂O or D₂O wt% was controlled by the weight ratio of Mg(OH)₂ or Mg(OD)₂ and MgO. Then each mixture was cold-sealed into the capsule to be compressed. For the EP12-6 run for iron-bearing hydrous ringwoodite we adopt a different procedure; powder of ground San Carlos olivine was first filled into the capsule, and liquid H₂O was injected into it. To avoid the leakage of H₂O, the capsule was spark-welded, weighed, kept in a vacuum for 1 h, and weighed again to confirm the weight was not changed by evaporation of H₂O.

These capsules were compressed using their relevant cell assembly, anvils, and load (Table 1). After the load reached the desired pressure, the capsule was heated by supplying and controlling the applied electric power. After the desired heating duration passed, the capsule was quenched to room temperature by cutting off the power. We established the power–temperature relations for each cell assembly by conducting several calibration runs in which the temperature of the sample capsule was monitored using a W₉₇Re₃/W₇₅Re₂₅ thermocouple inserted into the cell assembly and attached to the capsule. Reproducibility of the calibrated power–temperature relations was within ±5% and ±6% for the 8 and 6 mm TEL cell assembly, respectively. Temperatures of the actual synthesis runs were controlled using the supplied power derived from the calibrated power–temperature relations. No correction for the effect of pressure on the thermocouple electromotive force (emf) was applied.

The crystalline portion of the recovered run product from each synthesis experiment was divided into several samples of crystal aggregate. These pieces were first screened using a microfocus X-ray diffractometer (Rigaku RINT RAPID II) to find the mineral phases and to determine whether their Bragg reflections were powder-like rings or spotty. An incident X-ray beam of CuKα_{1,2} radiation operated

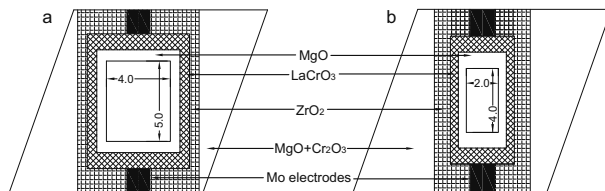


FIGURE 1. Cell assembly designs for pressure generation (a) to 21 GPa coupled with 8 mm truncation edge length (TEL) and (b) to 24 GPa coupled with 6 mm TEL. Sintered MgO–Cr₂O₃ pressure medium with octahedral edge length (OEL) = 14 mm were commonly used for these cells. Dimensions of the sample capsules are shown at the central areas of the cells.

at 40 kV and 30 mA was collimated onto a beam size of 100 µm for the analyses. The mineral grains were oscillated through movements of the omega and Φ axes, where X-ray diffraction patterns were taken in the reflection mode with an exposure time of 5–20 min. By using this screening process, we quickly evaluated whether the desired crystals with sizes larger than the collimator aperture were recovered. Then, crystallinities of selected samples were further evaluated individually by X-ray precession photography or SCXRD. A precession camera (Rigaku 1533A2) was used for several phase E, hydrogenated magnesian wadsleyite, and hydrogenated magnesian ringwoodite samples using MoKα_{1,2} radiation operating at 35 kV and 30 mA. Their reciprocal lattice images were taken on an imaging plate with an exposure time of 10 min. SCXRD measurements were conducted by using an automated four-circle X-ray diffractometer (Rigaku AFC-7s) with MoKα radiation (λ = 0.71073 Å) at the power of 50 kV and 30 mA. This instrument was used to measure crystals of deuterated magnesian ringwoodite and hydrogenated iron-bearing ringwoodite with dimensions of 80 × 50 × 50 µm³ and 80 × 70 × 50 µm³, respectively. A set of {511} X-ray reflections (24 in total) was used to refine the lattice constants of these ringwoodite crystals.

In addition, we evaluated the chemical heterogeneity of the recovered crystals. The crystals were polished with diamond powder 1 µm in size, coated with carbon, and analyzed using FE-SEM (JEOL JSM-7001F) and EPMA (JEOL JXA-8800). The electron beam was 5–10 µm in diameter, 15 kV in acceleration voltage, and 8–12 nA in current, which were adjusted with consideration to the varying fragility of the sample mineral phases. Analyses of backscattered electron (BSE) images of the crystals of all synthesized phases by FE-SEM revealed no evidence of chemical zoning. This result was confirmed by major element analyses of these crystals by EPMA, which are detailed subsequently in this paper.

Hydrogen and deuterium concentration distributions in the cross sections of phase E, deuterated magnesian ringwoodite, and hydrated iron-bearing ringwoodite crystals were measured by SIMS (CAMECA IMS-6F) at Hokkaido University. A primary ¹³³Cs⁺ beam operated at 9 nA and 10 kV was focused to a 10 µm spot on the sample, which was coated by gold 50 nm in thickness. Normal incident electron shower was used for electrostatic charge neutralization of sputtering area. The secondary negative ions of hydrogen, deuterium, and ³⁰Si were collected from the spattered area sequentially in an electron multiplier for 10 s. Small width of the exit slit was chosen to eliminate the ²⁸SiD interference on the ³⁰Si peak. For quantitative analysis, a natural amphibole containing 1.66 wt% of H₂O was used as a standard material (Miyagi and Yurimoto 1995). Both H₂O and D₂O contents in the samples were estimated assuming a linear relationship between their concentrations and the H/³⁰Si or D/³⁰Si ratio (Greenwood et al. 2011). Other measurement conditions were described elsewhere (Greenwood et al. 2011).

The space group and lattice parameters of the crystals, including those of all phase E, wadsleyite, and ringwoodite run products, were determined via analyses of the PXRD patterns using a few crystalline samples taken from each product (Table 2). All phase E, wadsleyite, and ringwoodite products were successfully indexed with *R*3̄*m*, *Imma*, and *Fd*3̄*m* space groups, respectively, which is consistent with previous structural analysis results. Water concentrations in wadsleyite and ringwoodite were estimated from their refined lattice constants (Jacobsen et al. 2005; Ye et al. 2012). In addition, whole sample products from the two phase E run charges were analyzed by TOF-NPD. The observed reflections in TOF-NPD were successfully indexed with the same *R*3̄*m* space group given by the PXRD results, and the linewidth profiles were analyzed to estimate the synthesis environments of these phase E products.

For PXRD analysis with the X-ray diffractometer (Rigaku Smartlab), each

crystal aggregate sample was ground into a fine powder in an alumina mortar and was measured on an Si low-background plate using the para-focusing method with $\text{CuK}\alpha$ radiation operated at 40 kV and 30 mA. The diffraction pattern was obtained by the step scanning method with a 2θ range of $10\text{--}140^\circ$, step size of 0.005° , and scan speed of $0.1\text{--}0.3^\circ/\text{min}$. The 2θ angles were calibrated by the silicon powder standard (NIST640d) as an external standard, and their lattice constants were refined through least-squares fitting of peak positions by using the UnitCell software (Holland and Redfern 1997). For TOF-NPD analysis, each sample was coarsely ground and measured using the TAKUMI Engineering Materials Diffractometer at Materials and Life Science Experimental Facility (MLF), Japan Proton Accelerator Research Complex (J-PARC) (Harjo et al. 2006). For the measurements, the optics of the neutron diffractometer were optimized for analyzing the structure of a hydrous mineral phase with a small sample mass (Okuchi et al. 2014).

RESULTS AND DISCUSSION

Figure 2 shows photographs of the recovered single crystals grown by the slow-cooling method. Observations of the samples under an optical microscope confirmed that these crystals had no visible imperfections. In the following sections, the results of microscopic analysis are given and are discussed in a comprehensive manner, demonstrating that these crystals were crystallographically and chemically homogeneous enough to be suitable for their expected usage. In addition, we show the most suitable experimental conditions for growing the largest crystals for each synthesized mineral phase.

DHMS phase E crystals

Single crystals of phase E up to $600\ \mu\text{m}$ in the largest dimension were synthesized in the two relevant experimental runs (Table 1, Fig. 2a). These crystals were significantly larger than the $100\text{--}200\ \mu\text{m}$ size previously reported (Kanzaki 1991; Kleppe et al. 2001; Kudoh et al. 1993). We found that the growth of phase E crystals was remarkably fast even at relatively low temperatures around $1100\ ^\circ\text{C}$; therefore, $2\text{--}3\ \text{h}$ of continuous heating at a constant temperature with a variation of less than $\pm 10\ ^\circ\text{C}$ was sufficient for recovering these large crystals. This fast crystal growth may be due in part to the very large water concentration ($\sim 22\ \text{wt}\%$) in the starting material, where below the silicate solidus, a large fraction of aqueous fluid coexisted with the crystals to facilitate the growth (Inoue 1994). It was observed that the capsules were completely filled with phase E crystals that were not sintered to each other, supporting that a large volume fraction of aqueous fluid had coexisted with the crystals.

Figure 3a shows a precession photograph of a representative crystal from the PE02 run of $270 \times 330 \times 530\ \mu\text{m}^3$. The diffraction spots of the phase E crystal are neither diffused nor split, which representatively demonstrates absences of stacking disorder and mosaicism in the product crystals. The major element composi-

tions in the cross sections of the other five crystals from the PE02 run showed a slight variation of $\text{Mg}/\text{Si} = 1.83 \pm 0.03$, which may include the effect of thermal gradient within the capsule (Fig. 4a). The refined lattice constants given in Table 2 were consistent with those reported in previous works determined by precise X-ray diffraction measurements, which expanded between $a = 2.9701(1)\ \text{\AA}$, $c = 13.882(1)\ \text{\AA}$ and $a = 2.9853(6)\ \text{\AA}$, $c = 13.9482(7)\ \text{\AA}$ (Kleppe et al. 2001; Kudoh et al. 1993). This variation may have been caused by the effects of the synthesis temperature in addition to the Mg/Si molar ratio of the starting materials. Considering the products starting only from $\text{Mg}/\text{Si} = 2$, the variation was reduced to between $a = 2.9701(1)\ \text{\AA}$, $c = 13.882(1)\ \text{\AA}$ for the sample synthesized at $1000\ ^\circ\text{C}$ (Kudoh et al. 1993), and $a = 2.975(1)\ \text{\AA}$, $c = 13.908(4)\ \text{\AA}$ for the sample synthesized at $1100\ ^\circ\text{C}$ (Kleppe et al. 2001). Assuming that this variation reflects only the temperature, we estimated the actual synthesis temperature for PE01 at $\sim 1060\ ^\circ\text{C}$ and PE02 at $\sim 960\ ^\circ\text{C}$ based on their lattice constants. The consistently lower temperatures by this estimation than the expected values of around $1100\ ^\circ\text{C}$ may be the result of an isotope effect because the lattice constants can shrink by deuteration, as in the case of brucite having a layered structure similar to that of phase E (Horita et al. 2010; Chakoumakos et al. 2013). We note that the observed occurrences of minor clinoenstatite in PXRD and TOF-NPD patterns of the phase E products in the present study are consistent with a temperature close to $1100\ ^\circ\text{C}$; otherwise, the clinoenstatite peaks would have disappeared (Inoue 1994). From these observations it is inferred that the lattice parameters are slightly different between deuterated and hydrogenated crystals synthesized at the same temperature, which is desirable to be more quantitatively evaluated by a future study to update the accuracy of temperature scale in the following discussion.

The thermal gradient within each sample capsule was approximated by using the above-mentioned lattice-to-temperature relation of the hydrogenated phase E. For this purpose, the full-width at half maximum (FWHM) of representative reflections in the whole-capsule TOF-NPD patterns was determined as a function of d -spacing (Fig. 5). Broadening by $\Delta d/d = 0.07\%$ and 0.10% , compared with the original resolution of the diffractometer, was observed for the PE01 and PE02 run charges, which correspond to the averaged thermal inhomogeneity of 40 and $60\ ^\circ\text{C}$ within the whole capsule, respectively. The thermal gradient is thus approximated to be $16\text{--}24$ or $20 \pm 4\ ^\circ\text{C}/\text{mm}$ for the $2.5\ \text{mm}$ length between the center and edge of the capsule shown in Figure 1a. We note that the observed FWHM values in TOF-NPD patterns were not increased by particle size and strain effects, because the sample grains are too large to have the size effect and are loosely

TABLE 2. Crystallographic parameters of the recovered crystals

Run no.	Phase	Space group	Lattice constants (\AA)			Unit-cell V_0 (\AA^3)	Water concentration (wt%)
			<i>a</i>	<i>b</i>	<i>c</i>		
PE01	phase E	$R\bar{3}m$	2.9731(1)		13.913(1)	106.50(1)	na
PE02	phase E	$R\bar{3}m$	2.9679(1)		13.888(1)	105.94(1)	1.0(1) (SIMS, H_2O), 6.9(5) (SIMS, D_2O)
EP13-2	Mg wadsleyite	<i>Imma</i>	5.6844(8)	11.527(2)	8.2532(7)	540.80(8)	1.6 (from <i>b/a</i>)
EP13-1	Mg wadsleyite	<i>Imma</i>	5.6852(4)	11.508(1)	8.2523(8)	539.92(10)	1.3 (from <i>b/a</i>)
HW7	Mg wadsleyite	<i>Imma</i>	5.6871(7)	11.512(2)	8.2568(8)	540.61(8)	1.3 (from <i>b/a</i>)
HW8	Mg wadsleyite	<i>Imma</i>	5.6879(6)	11.513(1)	8.2542(7)	540.55(8)	1.3 (from <i>b/a</i>)
HW18	Mg wadsleyite	<i>Imma</i>	5.6882(6)	11.497(1)	8.2554(8)	539.89(8)	1.1 (from <i>b/a</i>)
HR14	Mg ringwoodite	<i>Fd\bar{3}m</i>		8.0795(4)		527.41(8)	2.2(2) (from V_0)
HR12	Mg ringwoodite	<i>Fd\bar{3}m</i>	8.0773(3), 8.0771(5) ^a			526.99(6)	2.1(2) (from V_0), 0.6(1) (SIMS, H_2O), 0.5(0) (SIMS, D_2O)
EP13-3	Mg ringwoodite	<i>Fd\bar{3}m</i>		8.0834(2)		528.19(4)	2.6(2) (from V_0)
EP12-6	$\text{Mg}_{92}\text{Fe}_{08}$ ringwoodite	<i>Fd\bar{3}m</i>		8.0903(6) ^a		529.53(7)	2.0(2) (from V_0), 1.6(1) (SIMS, H_2O)

^a Determined by SCXRD.

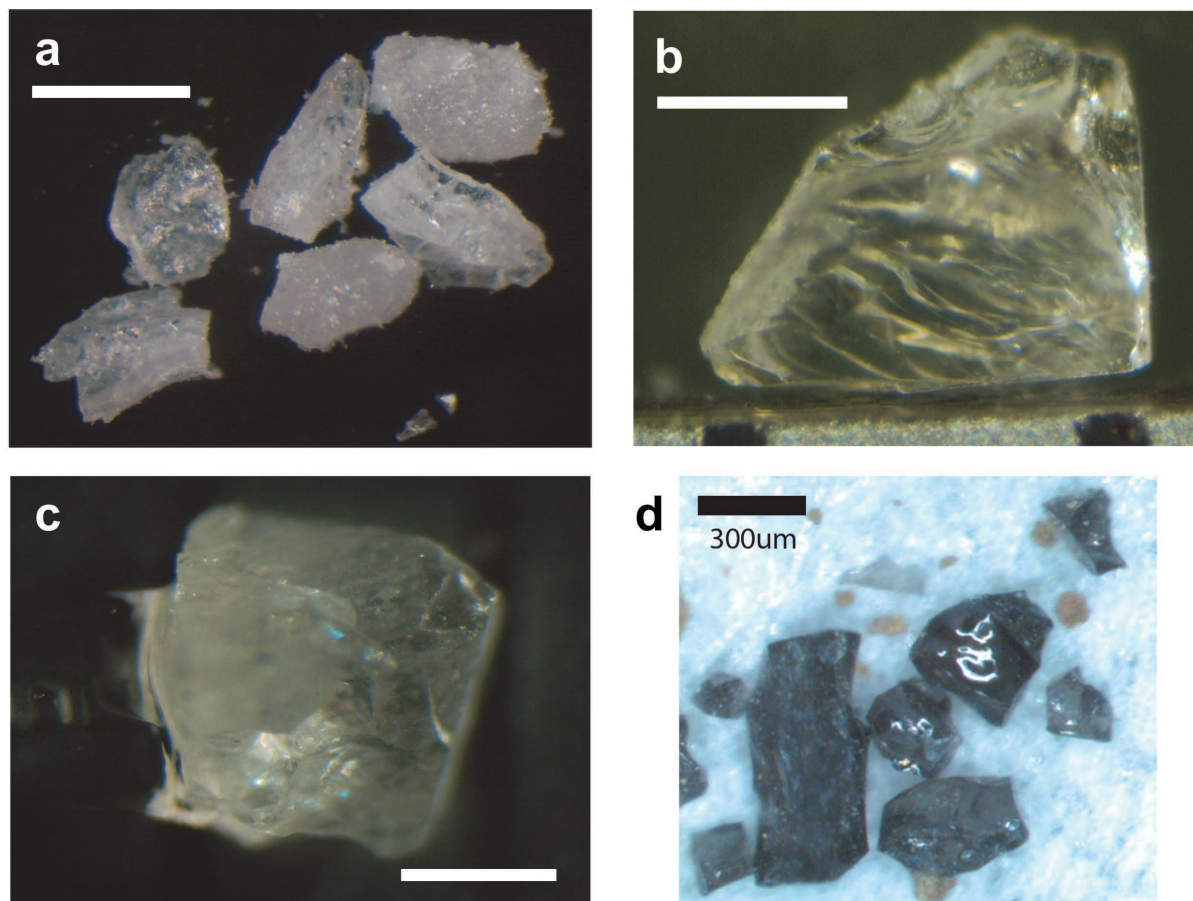


FIGURE 2. Photographs of representative crystals synthesized in and recovered from the high-pressure cells. Length of the scale bars is 500 μm unless explicitly shown. (a) Phase E from PE02; (b) hydrous magnesian wadsleyite from HR18; (c) hydrous magnesian ringwoodite from EP13-3; (d) iron-bearing bridgmanite from 5k2417.

packed into the sample holder without strain.

We finally discuss hydrogen isotopes of the synthesized phase E crystals. By SIMS analysis of the cross sections of five different crystals from the PE02 run, we found that the isotope abundance of hydrogen in these crystals was uniform at $D/(H + D) = 86 \pm 1\%$, and that total water concentration in these crystals showed little variation ($7.9 \pm 0.6 \text{ wt}\%$ as $\text{H}_2\text{O} + \text{D}_2\text{O}$; Fig. 6a). Considering these SIMS results in addition to the major element compositions by EPMA (Fig. 4a), it was confirmed that these deuterated phase E crystals are suitable for structure refinement or other studies that require chemical and isotopic homogeneity within their entire crystal volumes. The uniform hydrogen isotope abundance of 14% in all measured crystals indicates that hydrogen was contaminated into the crystals from sources outside of the capsule such as hydrogen released from an MgO sleeve or $\text{MgO}-\text{Cr}_2\text{O}_3$ pressure medium despite calcination at 1000 $^\circ\text{C}$ immediately prior to the cell construction and compression, because isotope abundance of hydrogen was less than 1% in the deuterated starting material in the capsule (Purevjav et al. 2014a). We are now conducting a structure refinement study of phase E from the TOF-NPD pattern of the PE02 sample having known hydrogen isotope abundance in this study (Tomioka et al. 2014).

Hydrous wadsleyite crystals

Single crystals of hydrous magnesian wadsleyite of 400–1100 μm in the largest dimensions were synthesized in the five relevant experimental runs (Table 1). The largest crystal size was $1100 \times 800 \times 800 \mu\text{m}^3$ (Fig. 2b), which is at least as large as the crystals previously synthesized using a thermal gradient (Shatskiy et al. 2009). From the results of these runs, we found that heating at around 1400 $^\circ\text{C}$ along with a reduction of 40 to 70 $^\circ\text{C}$ was the most effective temperature condition for growing large hydrous wadsleyite crystals, which is 200 to 300 $^\circ\text{C}$ higher than the wet solidus of the $\text{MgO}-\text{SiO}_2$ system (Inoue 1994). The observed melt fraction at this temperature reached about 70% in volume, where efficient buffering of crystal composition is expected to occur.

Figure 3b shows a precession photograph of a representative wadsleyite crystal from the EP13-2 run of $700 \times 500 \times 500 \mu\text{m}^3$, which demonstrates the high crystallinity of the product crystals. The major element compositions in the cross sections of the other three crystals from the EP13-2 run showed very little variation of $\text{Mg}/\text{Si} = 1.86 \pm 0.01$ (Fig. 4a), indicating that slow cooling of the crystals in large melt fraction is suitable for growing homogeneous hydrous wadsleyite crystals. These analyses also indicate that the thermal gradient of 20 $^\circ\text{C}/\text{mm}$, as estimated in the phase E runs,

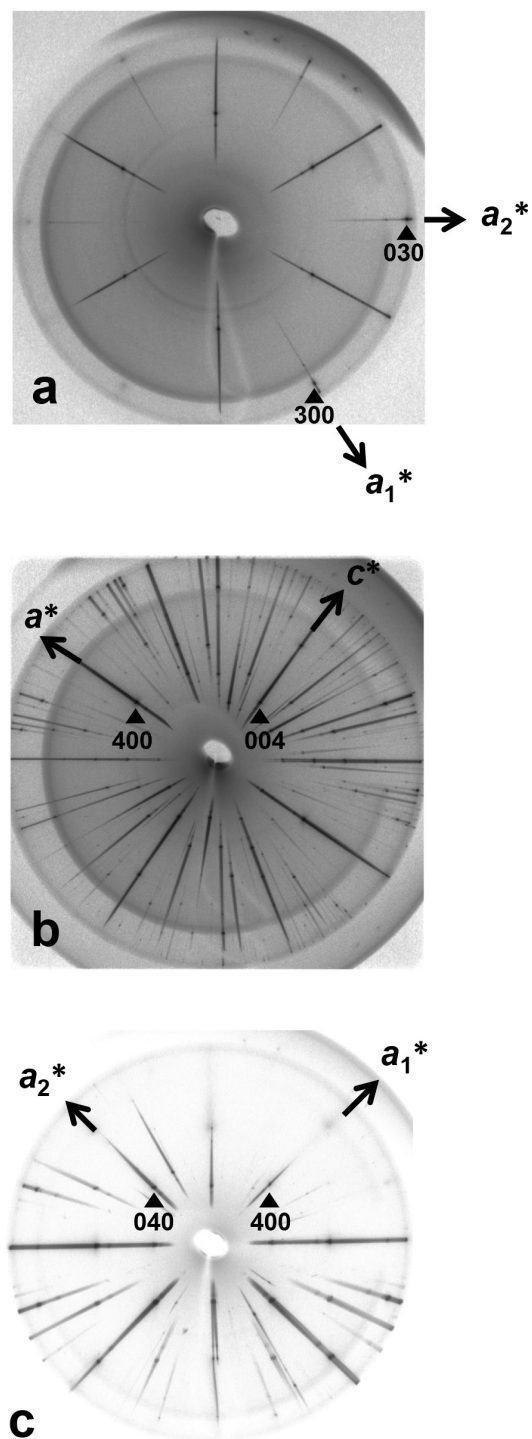


FIGURE 3. Precession X-ray diffraction photographs of the single crystals. (a) Phase E from PE02 along the [001] zone axis. (b) Hydrus wadsleyite from EP13-2 along the [010] zone axis. The weak extra spots come from small wadsleyite crystals associated with the host crystal. (c) Hydrus ringwoodite from EP13-3 along the [001] zone axis. Numbers denote Miller indices of diffraction spots indicated by arrows. All of the patterns show sharp diffraction spots from non-disordered single crystals.

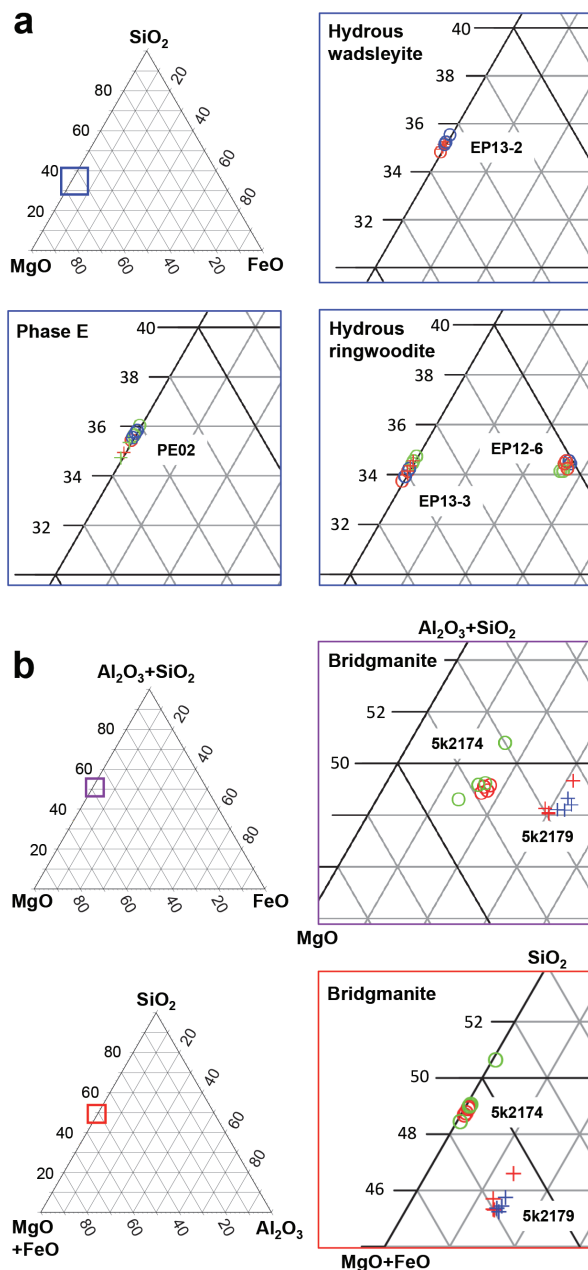


FIGURE 4. Major-element compositions of recovered single crystals taken by electron probe microanalyzer (EPMA). (a) Results from phase E (PE02), hydrus wadsleyite (EP13-2), and hydrus ringwoodite (EP12-6 and EP13-3) run charges plotted in ternary MgO–FeO–SiO₂ diagrams in molar ratio. (b) Results from MgFe-bearing bridgmanite (5k2174) and MgFeAl-bearing bridgmanite (5k2179) run charges plotted in ternary MgO–FeO–(Al₂O₃+SiO₂) and (MgO+FeO)–Al₂O₃–SiO₂ diagrams in molar ratio. These data plots are surrounded by the squares with blue, purple, or red color, which indicates that they are close-up views of the areas indicated by the corresponding colors in the entire triangle plots shown together. Each different color and symbol within these close-up views shows the EPMA results taken from each different crystal in the same run charge. The averaged chemical formula of MgFe- and MgFeAl-bearing bridgmanite crystals (5k2174 and 5k2179, excluding their H₂O components that were not analyzed) are Mg_{0.96}Fe_{0.07}Si_{0.98}O₃ and Mg_{0.90}Fe_{0.13}Al_{0.11}Si_{0.90}O₃, respectively.

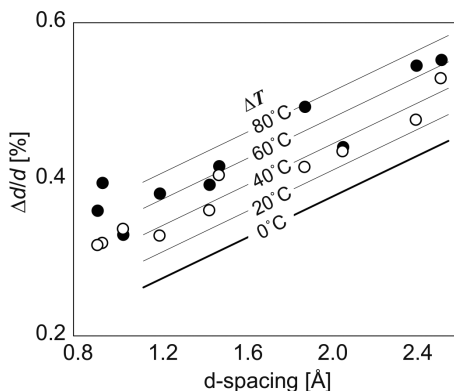


FIGURE 5. Relative neutron diffraction line width profiles $\Delta d/d$ of phase E as a function of d -spacing. Δd was defined as the full-width at half maximum (FWHM) of each reflection. Thin straight lines show expected $\Delta d/d$ positions when the described temperature inhomogeneity exists within the entire capsule (ΔT). Resolution of the diffractometer optics is shown by the bold line ($\Delta T = 0^\circ\text{C}$). Filled and open circles denote the results obtained for the entire PE01 and PE02 run charges, respectively. A Lorentz-type function was assumed for the line shape of the observed reflections, where the line width was approximated by the sum of that from the diffractometer optics and that from ΔT .

is too small to induce chemical heterogeneity in these crystals. The averaged H_2O concentration ($C_{\text{H}_2\text{O}}$) of wadsleyite in each run product including that from EP13-2 was separately estimated from each refined lattice constant (Table 2) using the established relation between the b/a ratio and $C_{\text{H}_2\text{O}}$ (Jacobsen et al. 2005). The estimated $C_{\text{H}_2\text{O}}$ had a variation between 1.6% for the EP13-2 run quenched at 1250°C and 1.1% for the HR-18 run quenched at 1320°C . These results are consistent with the reported systematics of $C_{\text{H}_2\text{O}} = 637e^{-0.0048T}$ (T in $^\circ\text{C}$), which accurately predicted 1.6 wt% at 1250°C and 1.1 wt% at 1320°C (Litasov et al. 2011).

A stark contrast of deuterium site positions between hydrous wadsleyite and hydrous ringwoodite has been reported by neutron diffraction of their deuterated powder samples (Purevjav et al. 2014; Sano-Furukawa et al. 2011). Whereas both structures commonly belong to spinel types, it was observed that deuterium in ringwoodite occupies both octahedral and tetrahedral sites, and that in wadsleyite occupies only an octahedral site. In other words, ringwoodite structure is uniquely vulnerable to exchanging silicon cations for hydrogen, which is much more effective for reducing sound velocity and increasing electrical conductivity than exchanging magnesium or iron cations for hydrogen (Mao et al. 2012; Panero et al. 2013). However, like the case for the current phase E sample, contamination of hydrogen was observed in the Raman spectrum of the wadsleyite powder, which might be the reason for smaller deuterium occupancy around the octahedral site (M3) than the estimation; the observed occupancy was only $\sim 75\%$ of the calculated value from D_2O concentration of the wadsleyite (Sano-Furukawa et al. 2011).

The problem of hydrogen contamination can be completely eliminated by using the crystals synthesized in the present study. Because the single-crystal diffraction method is in principle fully tolerable for incoherent scattering induced by hydrogen, crystals involving natural hydrogen isotopes are suitably analyzed without taking care of the contamination. Therefore, the hydrous wads-

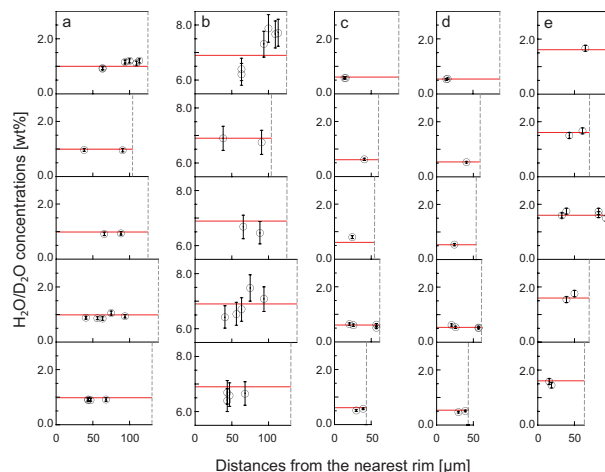


FIGURE 6. Secondary ion mass spectroscopy (SIMS) results of hydrogen and deuterium concentration distributions measured on polished cross sections of five representative crystals selected from each of the three representative run charges (15 crystals in total). (a and b) H_2O and D_2O concentrations of the deuterated phase E crystals recovered from the PE02 run, respectively. (c and d) H_2O and D_2O concentrations of the deuterated hydrous ringwoodite crystals recovered from the HR12 run, respectively. (e) H_2O concentration of hydrous ringwoodite crystals recovered from the EP12-6 run. The vertical scale shows recalculated H_2O or D_2O concentrations from their H^{30}Si or D^{30}Si ratios, respectively. To find compositional zoning or another heterogeneity within each crystal, the distances between each measurement position and the nearest rim of each cross section are shown in the horizontal scales. The broken lines show the distances from the center of each cross section to its nearest rim; note that actual dimension(s) of the measured crystals is larger than twice of these distances, because these are the observed minimum only within each cross section. The standard deviation of each water concentration value is estimated to be about 6% of the value (indicated by the error bars), which corresponds to the standard deviation of the measurement results of the hornblende H_2O standard (15 points in total). Red lines show averaged values within each sample capsule. D_2O within the PE02 and the HR12 crystal products were partly exchanged for H_2O during the crystal growth.

leyite crystal of sufficient size and homogeneity in the present study has been measured at TOPAZ instrument at SNS without any problem. Whereas full structure refinement of this wadsleyite crystal is currently in progress, it was preliminarily shown that hydrogen occupancy in the M3 site is much closer to the value estimated from $C_{\text{H}_2\text{O}}$ of the crystal (Purevjav et al. 2014b). We will report the refinement result elsewhere in the near future.

Hydrous ringwoodite crystals

Single crystals of hydrous ringwoodite of up to $1000\ \mu\text{m}$ were synthesized in the four relevant experimental runs (Table 1). Figure 2c shows one of the largest crystals from the EP13-3 run, which to the best of our knowledge is greater than any size reported in previous research. Such growth of ringwoodite requires a larger reduction in temperature (by 110°C) compared with that in the case of wadsleyite. The other runs with smaller changes in temperature (HR14) or constant temperatures (HR12 and EP12-6) resulted in smaller sizes, between 200 and $600\ \mu\text{m}$. These ringwoodite crystals were grown between 1260 and 1400°C , where they were observed to coexist with silicate melt, as expected from the relevant phase

relations (Ohtani et al. 2000). For the EP13-3 run, we observed that about half of the sample volume was melted, whereas the other runs had smaller melt fractions. It was demonstrated from these observations that the growth rate changed largely with time. The rate was very rapid during initial crystallization and then became slower and slower during subsequent recrystallization with the melt-crystal interface kept close to the chemical equilibrium. The growth rate in the latter stage was moderately enhanced by precipitation of crystal volume upon reduction of the temperature, and an effective combination of these two processes made it possible to produce the single crystals of ringwoodite of 1 mm size in the EP13-3 run.

A precession photograph of the crystal shown in Figure 2c was captured along the [001] direction (Fig. 3c). The photograph shows sharp diffraction spots, and no extra spot was observed. Moreover, SCXRD results of the two ringwoodite crystals taken from the HR12 and EP12-6 runs showed no intensity for the forbidden reflections, and no effect of twinning on their X-ray intensity data. The major element compositions in the cross sections of five crystals from the EP12-6 run and four crystals from the HR13-3 run showed little variations of Mg/Si = 1.92 ± 0.01 and (Mg+Fe)/Si = 1.93 ± 0.02 , respectively (Fig. 4a). These results indicate that slow cooling of the crystals in large melt fraction is suitable for growing homogeneous ringwoodite crystals. Using the refined lattice constants of the ringwoodite crystals by PXRD and SCXRD, the $C_{\text{H}_2\text{O}}$ of each run product was estimated along the relation between unit-cell volume V_0 and $C_{\text{H}_2\text{O}}$ (Ye et al. 2012). The estimated $C_{\text{H}_2\text{O}}$ were between 2.0 and 2.6 wt% (Table 2), which were close to the uppermost values of previously observed $C_{\text{H}_2\text{O}}$ in hydrous ringwoodite (Inoue et al. 1998; Kudoh et al. 2000; Ye et al. 2012). It is suggested that the $C_{\text{H}_2\text{O}}$ in ringwoodite increases with increasing synthesis duration; the highest $C_{\text{H}_2\text{O}}$ of 2.6% among the current crystal products was synthesized after 12 h of heating, which is indeed the most lengthy among all synthesis experiments of the hydrous ringwoodite. The following SIMS results show no evidence of zoning of $C_{\text{H}_2\text{O}}$, so that the increase of $C_{\text{H}_2\text{O}}$ with time is not because of diffusion of H_2O into the ringwoodite crystals after their growth. Another possible process such as Mg^{2+} - Si^{4+} site disorder involving hydrogen may be additionally considered (Kudoh et al. 2000).

Hydrogen isotope concentrations were analyzed by SIMS for the polished cross sections of several ringwoodite crystals from the HR12 and EP12-6 runs. Although the HR12 product crystals were synthesized from fully deuterated starting materials, it was proved to have been extensively exchanged with hydrogen having natural isotope abundance. The isotope abundance of hydrogen was uniformly distributed at $\text{D}/(\text{H} + \text{D}) = 45 \pm 3\%$ among all five crystals from the HR12 run (Fig. 6). As in the case of phase E synthesis, such incorporation of outside hydrogen most likely occurred through its diffusion from outside of the capsule, which is inevitably more extensive for the ringwoodite synthesized at a temperature 300 °C higher than that for the phase E. It is therefore concluded that complete deuteration of ringwoodite crystals using the current cell design and experimental condition is difficult. On the other hand, the EP12-6 products were synthesized from starting materials containing hydrogen with natural isotope abundance. The five measured crystals consistently showed a very uniform hydrogen concentration of 1.6 ± 0.1 wt% (Fig. 6). By all these ana-

lytical results, it was demonstrated that the slow-cooling method is suitable for growing homogeneously hydrous ringwoodite crystals that are appropriate for TOF single-crystal diffraction.

Bridgmanite crystals

Single crystals of bridgmanite with three different composition types were synthesized in the five relevant experimental runs (Table 1). The largest were iron-bearing bridgmanite crystals from the 5k2417 run at up to 600 μm in the largest dimension (Fig. 2d). These crystals were grown from the starting materials having silicate compositions between $(\text{Mg,Fe})_2\text{SiO}_4$ and $(\text{Mg,Fe})\text{SiO}_3$, which are effective for preventing stishovite crystal inclusions (Shatskiy et al. 2007). Moreover, existence of H_2O significantly facilitates the crystal growth of bridgmanite (Ito and Weidner 1986; Shatskiy et al. 2007). The BSE image of these crystals showed their high homogeneity (Fig. 7), which is consistent with the major element compositions measured in the cross sections of several different crystals from two experimental runs 5k2174 and 5k2179 (Fig. 4b). These results indicated that the slow cooling in water-bearing conditions is certainly effective for growing homogeneous bridgmanite crystals of moderate sizes, while it is still necessary to improve the cell design and experimental conditions for growing the crystals 1 mm in size.

We confirmed the existence of hydrous silicate melt at temperature conditions of 1650 to 1760 °C, from which crystal growth occurred in the present study. This is consistent with the reported phase relations at hydrous condition (Ito and Weidner 1986; Ohtani et al. 2000). We found that fine-tuning of the initial temperature and the extent of its decrease is not essential for increasing the crystal size, whereas a longer heating duration is definitely effective. From these observations it is inferred that recrystallization during the lengthy heating is a more effective process for increasing crystal size of bridgmanite, compared with growth through crystal precipitation from the melt by reduction of temperature. In addition, it was demonstrated that sizes of aluminous bridgmanite crystals from the 5k2179 run were smaller than those of non-aluminous

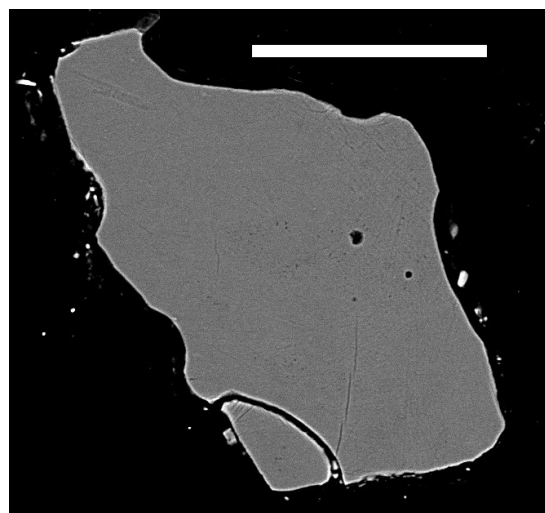


FIGURE 7. Backscattering electron (BSE) image of polished cross section of an iron-bearing bridgmanite crystal from 5k2417. The scale bar is 100 μm in length.

bridgmanite from the other runs. It was recently reported that such aluminous bridgmanite synthesized in hydrous conditions contains a significant amount of H₂O up to almost 1 wt% (Inoue et al. 2012), whereas non-aluminous bridgmanite grown in hydrous conditions contains only a few hundred parts per million of H₂O (Litasov et al. 2003; Shatskiy et al. 2007). Apparently, a considerable amount of future study is required for growing highly hydrous, alumina-bearing bridgmanite crystals suitable for analysis of hydrogen by single-crystal neutron diffraction.

The thermal gradient in the growth environment for the bridgmanite (Fig. 1b) is presumably comparable to or smaller than that for the phase E, wadsleyite, or ringwoodite (Fig. 1a), because the capsule dimensions were smaller and the thermal insulator was about 70% thicker. In addition, at the significantly higher temperature conditions used for the bridgmanite synthesis, more efficient radiative heat transfer was expected along the semi-transparent MgO sleeve body, which had an increased grain size after the lengthy heating (Hofmeister 2005). Although we cannot evaluate the actual gradient in a quantitative manner, the expectation was qualitatively consistent with the observed crystal shape of bridgmanite. The shape was mostly euhedral throughout the entire capsule volume of all five runs, rather than the fan-shaped, needle-like aggregate type synthesized in the cells with thermal gradients significantly larger than 20 °C/mm (Ito and Weidner 1986; Shatskiy et al. 2007).

We finally note that a part of the bridgmanite crystal products in the present study has been successfully applied for in situ radiative thermal conductivity measurements via optical absorption spectroscopy in a high-pressure diamond-anvil cell (Goncharov et al. 2015). We are also planning to utilize these crystals for high-pressure studies of electronic spin and valence states of iron in the lower-mantle bridgmanite using synchrotron X-ray emission and Mössbauer spectroscopy, in addition to single-crystal elasticity measurements of iron-bearing bridgmanite in the lower mantle using impulsive stimulated light scattering and Brillouin light scattering.

IMPLICATIONS

It has been demonstrated that slow cooling in a Kawai-type cell is the best suitable method to synthesize homogeneous silicate crystals of 600 to 1100 μm sizes at pressures up to 24 GPa. Degree of temperature reduction to facilitate the growth needs to be evaluated and optimized for each phase. Loeffert et al. (2002) used the slow-cooling method at 6 GPa in a belt press to grow a SrCu₂O₃ crystal 2 mm in size. The method in the present study should be applicable for the crystal growth of such an oxide phase at pressures at least up to 20 GPa; it may provide a new application of the Kawai cell in the field of material sciences by exploiting its high thermal stability and controllability at such pressure regime.

For applications of the product crystals in the present study, we emphasize that synthetic single crystals at very high pressures have now become measurable by neutron diffraction. The result is newly allowing us to determine a hydrogen site occupancy of the contamination-free crystal in terms of isotopes. Moreover, TOF single-crystal diffraction instruments provide about twice or even higher spatial resolution than previously used powder instruments; D20 at Institut Laue-Langevin was used at $d_{\min} = 0.96 \text{ \AA}$ for analyzing the deuterated wadsleyite powder (Sano-Furukawa et al. 2011), whereas TOPAZ was used at $d_{\min} = 0.50 \text{ \AA}$ (Schultz

et al. 2014) and SXD at ISIS was used at $d_{\min} = 0.31 \text{ \AA}$ (Artioli et al. 1995) for analyzing single-crystal samples. The significantly smaller d_{\min} by these TOF single-crystal instruments is because it is the best sensitive scheme for detecting diffraction at small d -values, which are induced by neutrons of short wavelengths. Thus, the geometry of chemical bonding around a hydrogen atom in the deep-mantle hydrous minerals, including the distances of covalent and hydrogen bonding and the angle between them, are determined with significantly higher accuracy. Using these we will critically evaluate the proposed relations between the bonding geometry and Raman and infrared spectra of hydrogen, which includes that recently proposed by Panero et al. (2013) and their referred previous studies. Bonding geometries predicted by previous theoretical calculations of deep-mantle hydrogen will also be evaluated.

We finally note that all crystals in each sample capsule in the present study have a uniform chemical composition. Therefore, lattice parameters, water concentration, and major element compositions of a candidate crystal can be promptly evaluated by PXRD and EPMA results of the other crystals without destroying the candidate itself, which make it easy and straightforward to select the best sample for single-crystal diffraction. Such a pre-evaluation is essential to avoid wasting invaluable neutron beam time by measuring an inappropriate crystal.

ACKNOWLEDGMENTS

This work was supported by JSPS grants-in-aid for Scientific Research (No. 23340161, 23540558, and 26287135). Visits to the Institute for Study of the Earth's Interior by J.F. Lin, L. Schoneveld, and H. Hwang were supported by a special grant from the Ministry of Education, Culture, Sports, Science and Technology. Part of the research conducted at J-PARC was through MLF user program (No. 2012B0016), where S. Harjo and J. Abe are acknowledged for technical supports. Part of the research conducted at SNS, Oak Ridge National Laboratory was sponsored by the Scientific User Facilities Division, Office of Basic Energy Sciences, U.S. Department of Energy, where C. Hoffman and X. Wang are acknowledged for technical supports. T. Okuchi acknowledges support from X-ray Free Electron Laser Priority Strategy Program (MEXT) for part of the research. J.F. Lin acknowledges support from the U.S. National Science Foundation Geophysics Program (NSF EAR Early Career), Energy Frontier Research in Extreme Environments (EFree), and Center for High Pressure Science and Advanced Technology (HPSTAR) for part of the research. The authors thank Chikako Oka and Eiji Ito for technical supports and discussion in conducting Kawai-type experiments, Megan Matheny for manuscript editing, and Anton Shatskiy and one anonymous reviewer for providing constructive comments to improve the manuscript.

REFERENCES CITED

- Artioli, G., Rinaldi, R., Wilson, C.C., and Zanazzi, P.F. (1995) Single-crystal pulsed neutron diffraction of a highly hydrous beryl. *Acta Crystallographica*, B51, 733–737.
- Bercovici, D., and Karato, S. (2003) Whole-mantle convection and the transition-zone water filter. *Nature*, 425, 39–44.
- Bolfan-Casanova, N., Keppler, H., and Rubie, D.C. (2000) Water partitioning between nominally anhydrous minerals in the MgO–SiO₂–H₂O system up to 24 GPa: Implications for the distribution of water in the Earth's mantle. *Earth and Planetary Science Letters*, 182, 209–221.
- Chakoumakos, B.C., Horita, J., and Garlea, V.O. (2013) H/D isotope effects in brucite at low temperatures. *American Mineralogist*, 98, 1–6.
- Chen, J.H., Inoue, T., Weidner, D.J., Wu, Y.J., and Vaughan, M.T. (1998) Strength and water weakening of mantle minerals, olivine, wadsleyite and ringwoodite. *Geophysical Research Letters*, 25, 575–578.
- Frost, D.J., Poe, B.T., Trønnes, R.G., Liebske, C., Duba, A., and Rubie, D.C. (2004) A new large-volume multianvil system. *Physics of the Earth and Planetary Interiors*, 143–144, 507–514.
- Ghosh, S., Ohtani, E., Litasov, K.D., Suzuki, A., Dobson, D., and Funakoshi, K. (2013) Effect of water in depleted mantle on post-spinel transition and implication for 660 km seismic discontinuity. *Earth and Planetary Science Letters*, 371, 103–111.
- Goncharov, A.F., Lobanov, S.S., Tan, X., Hohensee, T., Cahill, D.G., Lin, J.F., Thomas, S.M., Okuchi, T., and Tomioka, N. (2015) Experimental study of thermal conductivity at high pressures: Implications for the deep Earth's interior. *Physics of the Earth and Planetary Interiors*, in press, <http://dx.doi.org/10.1016/j.pepi.2015.02.004>.

- Greenwood, J.P., Itoh, S., Sakamoto, N., Warren, P., Taylor, L., and Yurimoto, H. (2011) Hydrogen isotope ratios in lunar rocks indicate delivery of cometary water to the Moon. *Nature Geoscience*, 4, 79–82.
- Harjo, S., Moriai, A., Torii, S., Suzuki, H., Suzuya, K., Morii, Y., Arai, M., Tomota, Y., Akita, K., and Akiniwa, Y. (2006) Design of engineering diffractometer at J-PARC. *Materials Science Forum*, 524–529, 199–204.
- Hofmeister, A.M. (2005) Dependence of diffusive radiative transfer on grain-size, temperature, and Fe-content: Implications for mantle processes. *Journal of Geodynamics*, 40, 51–72.
- Holland, T.J.B., and Redfern, S.A.T. (1997) Unit cell refinement from powder diffraction data: The use of regression diagnostics. *Mineralogical Magazine*, 61, 65–77.
- Horita, J., dos Santos, A., Tulk, C., Chakoumakos, B., and Polyakov, V. (2010) High-pressure neutron diffraction study on H–D isotope effects in brucite. *Physics and Chemistry of Minerals*, 37, 741–749.
- Inoue, T. (1994) Effect of water on melting phase relations and melt composition in the system Mg_2SiO_4 - $MgSiO_3$ - H_2O up to 15 GPa. *Physics of the Earth and Planetary Interiors*, 85, 237–263.
- Inoue, T., Yurimoto, H., and Kudoh, Y. (1995) Hydrous modified spinel, $Mg_{1.75}SiH_{0.5}O_4$: a new water reservoir in the mantle transition region. *Geophysical Research Letters*, 22, 117–120.
- Inoue, T., Weidner, D.J., Northrup, P.A., and Parise, J.B. (1998) Elastic properties of hydrous ringwoodite (γ -phase) in Mg_2SiO_4 . *Earth and Planetary Science Letters*, 160, 107–113.
- Inoue, T., Wada, T., Sasaki, R., and Yurimoto, H. (2010) Water partitioning in the Earth's mantle. *Physics of the Earth and Planetary Interiors*, 183, 245–251.
- Inoue, T., Yabuki, T., and Yurimoto, H. (2012) Water contents of Al-bearing minerals in the mantle transition zone and the lower mantle. In T. Okuchi, Ed., *Joint Symposium of Misasa-2012 and Geofluid-2*, p. P21-02. ISEI, Misasa, Tottori, Japan.
- Ito, E., and Weidner, D.J. (1986) Crystal growth of $MgSiO_3$ perovskite. *Geophysical Research Letters*, 13, 464–466.
- Jacobsen, S.D., Smyth, J.R., Spetzler, H., Holl, C.M., and Frost, D.J. (2004) Sound velocities and elastic constants of iron-bearing hydrous ringwoodite. *Physics of the Earth and Planetary Interiors*, 143–144, 47–56.
- Jacobsen, S.D., Demouchy, S., Frost, D.J., Ballaran, T.B., and Kung, J. (2005) A systematic study of OH in hydrous wadsleyite from polarized FTIR spectroscopy and single-crystal X-ray diffraction: Oxygen sites for hydrogen storage in Earth's interior. *American Mineralogist*, 90, 61–70.
- Jørgensen, M.R.V., Hathwar, V.R., Sist, M., Wang, X., Hoffmann, C.M., Briseno, A.L., Overgaard, J., and Iversen, B.B. (2014) Accurate atomic displacement parameters from time-of-flight neutron-diffraction data at TOPAZ. *Acta Crystallographica*, A70, 679–681.
- Kanzaki, M. (1991) Stability of hydrous magnesium silicates in the mantle transition zone. *Physics of the Earth and Planetary Interiors*, 66, 307–312.
- Keppeler, H., and Smyth, J.R. (2006) Water in Nominally Anhydrous Minerals. *Reviews in Mineralogy and Geochemistry*, 62, 478 p.
- Kleppe, A.E., Jephcoat, A.P., and Ross, N.L. (2001) Raman spectroscopic studies of phase E to 19 GPa. *American Mineralogist*, 86, 1275–1281.
- Kohlstedt, D.L., Keppeler, H., and Rubie, D.C. (1996) Solubility of water in the alpha, beta and gamma phases of $(Mg,Fe)_2SiO_4$. *Contributions to Mineralogy and Petrology*, 123, 345–357.
- Kubo, T., Ohtani, E., Kato, T., Shimmei, T., and Fujino, K. (1998) Effects of water on the α - β transformation kinetics in San Carlos olivine. *Science*, 281, 85–87.
- Kudoh, Y., Finger, L.W., Hazen, R.M., Prewitt, C.T., Kanzaki, M., and Veblen, D.R. (1993) Phase E: A high pressure hydrous silicate with unique crystal chemistry. *Physics and Chemistry of Minerals*, 19, 357–360.
- Kudoh, Y., Kuribayashi, T., Mizobata, H., and Ohtani, E. (2000) Structure and cation disorder of hydrous ringwoodite, γ - $Mg_{1.89}Si_{0.98}H_{0.30}O_4$. *Physics and Chemistry of Minerals*, 27, 474–479.
- Litasov, K., Ohtani, E., Langenhorst, F., Yurimoto, H., Kubo, T., and Kondo, T. (2003) Water solubility in Mg-perovskites, and water storage capacity in the lower mantle. *Earth and Planetary Science Letters*, 211, 189–203.
- Litasov, K., Shatskiy, A., Ohtani, E., and Katsura, T. (2011) Systematic study of hydrogen incorporation into Fe-free wadsleyite. *Physics and Chemistry of Minerals*, 38, 75–84.
- Loeffler, A., Gross, C., and Assmus, W. (2002) Crystal growth under high pressure: Preparation of the spin-ladder compound $SrCu_2O_3$. *Journal of Physics: Condensed Matter*, 14, 11161.
- Mao, Z., Jacobsen, S.D., Frost, D.J., McCammon, C.A., Hauri, E.H., and Duffy, T.S. (2011) Effect of hydrogen on the single-crystal elasticity of Fe-bearing wadsleyite to 12 GPa. *American Mineralogist*, 96, 1606–1612.
- Mao, Z., Lin, J.-F., Jacobsen, S.D., Duffy, T.S., Chang, Y.-Y., Smyth, J.R., Frost, D.J., Hauri, E.H., and Prakapenka, V.B. (2012) Sound velocities of hydrous ringwoodite to 16 GPa and 673 K. *Earth and Planetary Science Letters*, 331–332, 112–119.
- McCammon, C.A., Frost, D.J., Smyth, J.R., Laustsen, H.M.S., Kawamoto, T., Ross, N.L., and van Aken, P.A. (2004) Oxidation state of iron in hydrous mantle phases: implications for subduction and mantle oxygen fugacity. *Physics of the Earth and Planetary Interiors*, 143, 157–169.
- Miyagi, I., and Yurimoto, H. (1995) Water content of melt inclusions in phenocrysts using secondary ion mass spectrometer. *Bulletin of the Volcanological Society of Japan*, 40, 349–355.
- Mrosko, M., Lenz, S., McCammon, C.A., Taran, M., Wirth, R., and Koch-Muller, M. (2013) Hydrogen incorporation and the oxidation state of iron in ringwoodite: A spectroscopic study. *American Mineralogist*, 98, 629–636.
- Ohtani, E., Mizobata, H., and Yurimoto, H. (2000) Stability of dense hydrous magnesium silicate phases in the systems Mg_2SiO_4 - H_2O and $MgSiO_3$ - H_2O at pressures up to 27 GPa. *Physics and Chemistry of Minerals*, 27, 533–544.
- Ohtani, E., Litasov, K., Hosoya, T., Kubo, T., and Kondo, T. (2004) Water transport into the deep mantle and formation of a hydrous transition zone. *Physics of The Earth and Planetary Interiors*, 143–144, 255–269.
- Okuchi, T. (1997) Hydrogen partitioning into molten iron at high pressure: Implications for Earth's core. *Science*, 278, 1781–1784.
- Okuchi, T., Tomioka, N., Purevjav, N., Abe, J., Harujo, S., and Gong, W. (2014) Structure refinement of sub-cubic-mm volume sample at high pressures by pulsed neutron powder diffraction: application to brucite in an opposed anvil cell. *High Pressure Research*, 34, 273–280.
- Panero, W.R., Smyth, J.R., Pigott, J.S., Liu, Z.X., and Frost, D.J. (2013) Hydrous ringwoodite to 5 K and 35 GPa: Multiple hydrogen bonding sites resolved with FTIR spectroscopy. *American Mineralogist*, 98, 637–642.
- Pearson, D.G., Brenker, F.E., Nestola, F., McNeill, J., Nasdala, L., Hutchison, M.T., Matveev, S., Mather, K., Silversmit, G., Schmitz, S., Vekemans, B., and Vincze, L. (2014) Hydrous mantle transition zone indicated by ringwoodite included within diamond. *Nature*, 507, 221–224.
- Purevjav, N., Okuchi, T., Tomioka, N., Abe, J., and Harujo, S. (2014a) Hydrogen site analysis of hydrous ringwoodite in mantle transition zone by pulsed neutron diffraction. *Geophysical Research Letters*, 41, 6718–6724.
- Purevjav, N., Okuchi, T., Tomioka, N., Hoffmann, C., and X. Wang. (2014b) Unique substitution mechanism of hydrogen in deep mantle wadsleyite demonstrated by time of flight single-crystal Laue diffraction. *Japanese Society of Neutron Science 2014 Annual Meeting Abstract Volume*, Sapporo, Japan.
- Rudolph, P. (2010) Defect formation during crystal growth from the melt. In G. Dhanaraj, K. Byrappa, V. Prasad, and M. Dudley, Eds., *Springer Handbook of Crystal Growth*, 159–201. Springer, Berlin.
- Sano-Furukawa, A., Kuribayashi, T., Komatsu, K., Yagi, T., and Ohtani, E. (2011) Investigation of hydrogen sites of wadsleyite: A neutron diffraction study. *Physics of the Earth and Planetary Interiors*, 189(1–2), 56–62.
- Schmandt, B., Jacobsen, S.D., Becker, T.W., Liu, Z.X., and Dueker, K.G. (2014) Dehydration melting at the top of the lower mantle. *Science*, 344, 1265–1268.
- Schultz, A.J., Jørgensen, M.R.V., Wang, X., Mikkelsen, R.L., Mikkelsen, D.J., Lynch, V.E., Peterson, P.F., Green, M.L., and Hoffmann, C.M. (2014) Integration of neutron time-of-flight single-crystal Bragg peaks in reciprocal space. *Journal of Applied Crystallography*, 47, 915–921.
- Shatskiy, A., Fukui, H., Matsuzaki, T., Shinoda, K., Yoneda, A., Yamazaki, D., Ito, E., and Katsura, T. (2007) Growth of large (1 mm) $MgSiO_3$ perovskite single crystals: A thermal gradient method at ultrahigh pressure. *American Mineralogist*, 92, 1744–1749.
- Shatskiy, A., Litasov, K.D., Matsuzaki, T., Shinoda, K., Yamazaki, D., Yoneda, A., Ito, E., and Katsura, T. (2009) Single crystal growth of wadsleyite. *American Mineralogist*, 94, 1130–1136.
- Shatskiy, A., Yamazaki, D., Borzdov, Y.M., Matsuzaki, T., Litasov, K., Cooray, T., Ferot, A., Ito, E., and Katsura, T. (2010) Stishovite single-crystal growth and application to silicon self-diffusion measurements. *American Mineralogist*, 95, 135–143.
- Shatskiy, A., Katsura, T., Litasov, K.D., Shcherbakova, A.V., Borzdov, Y.M., Yamazaki, D., Yoneda, A., Ohtani, E., and Ito, E. (2011) High pressure generation using scaled-up Kawai-cell. *Physics of the Earth and Planetary Interiors*, 189, 92–108.
- Shibazaki, Y., Ohtani, E., Terasaki, H., Suzuki, A., and Funakoshi, K. (2009) Hydrogen partitioning between iron and ringwoodite: Implications for water transport into the Martian core. *Earth and Planetary Science Letters*, 287, 463–470.
- Smyth, J.R., Holl, C.M., Frost, D.J., Jacobsen, S.D., Langenhorst, F., and McCammon, C.A. (2003) Structural systematics of hydrous ringwoodite and water in Earth's interior. *American Mineralogist*, 88, 1402–1407.
- Smyth, J.R., Boffan-Casanova, N., Avignand, D., El-Ghoozi, M., and Hirner, S.M. (2014) Tetrahedral ferric iron in oxidized hydrous wadsleyite. *American Mineralogist*, 99, 458–466.
- Tamura, S., Kato, K., and Goto, M. (1974) Single crystals of $T-Nb_2O_5$ obtained by slow cooling method under high pressures. *Zeitschrift für anorganische und allgemeine Chemie*, 410, 313–315.
- Tomioka, N., Okuchi, T., and Purevjav, N. (2014) Pulsed neutron diffraction study of dense hydrous magnesium silicate phase E. DE5-A, International Mineralogical Association 2014, Gauteng, South Africa.
- Wenk, H.-R. (2006) Neutron Scattering in Earth Sciences. *Reviews in Mineralogy and Geochemistry*, Mineralogical Society of America, 63, 471 p.
- Yang, X.Z., Keppeler, H., Dubrovinsky, L., and Kurnosov, A. (2014) In-situ infrared spectra of hydroxyl in wadsleyite and ringwoodite at high pressure and high temperature. *American Mineralogist*, 99, 724–729.
- Ye, Y., Brown, D.A., Smyth, J.R., Panero, W.R., Jacobsen, S.D., Chang, Y.Y., Townsend, J.P., Thomas, S.M., Hauri, E.H., Dera, P., and Frost, D.J. (2012) Compressibility and thermal expansion of hydrous ringwoodite with 2.5(3) wt% H_2O . *American Mineralogist*, 97, 573–582.